CHAPTER III
HYBRID PARTICLE TRACKING VELOCIMETRY AND THREE-DIMENSIONAL VELOCITY FIELD RECONSTRUCTION

Although many two-phase flow measurement techniques exist in the chemical, petroleum and nuclear industries (Ishii & Theofanous 1998), and many of the different patterns in a two-phase flow have been studied, there still exists a lack of information and understanding of the physical phenomena. Basic hydrodynamics, mixing, mass and heat transport have not been described based on first principles. Traditionally, design and scale-up of the systems are largely based on empirical models. In these models, the design parameters are largely evaluated by correlations that are applicable to narrow operating ranges. A good knowledge of the structure of the flow, including the behavior of the individual phases and the pattern of the flow, is important in areas as safety of the nuclear power plants and efficient design of other industrial systems.

A brief description of the physical fundaments of the particle image velocimetry flow measurement technique is presented in this chapter. Then, a short description of the Adaptive Resonance Theory 2 Neural Network (ART2 NN) and the Spring Model tracking techniques, and their combination to form the hybrid tracking technique used in this investigation, is shown. Finally, the method to determine the third dimension from a stereo pair of images is described.

3.1. Pulsed-light velocimetry

Pulsed-light velocimetry (PLV) is a flow-field measurement technique, in which the images of small markers freely flowing in the fluid under study are acquired at two, or more, different times, by pulsing some light source (Adrian 1991). The motion of the markers is then a measure of the motion of the fluid under study, and, consequently, a whole flow field composed of many local velocities $\mathbf{u}$, at different locations in the fluid, can be estimated from:

$$\mathbf{u}(\mathbf{x},t) = \frac{\Delta \mathbf{x}(\mathbf{x},t)}{\Delta t}, \qquad [7]$$

where $\Delta \mathbf{x}$ is the marker position change in the time interval Δt.

The markers used to follow the fluid motion can be solid particles, gas bubbles, liquid droplets, or patches of molecules, among others. The images of these markers are acquired by photographic cameras and/or electronic cameras, and are recorded on photographic film, couple charged device (CCD) detector arrays, holographic plates, etc. Depending on the kind of markers to be used in the measurement, PLV is divided into two categories: particulate markers, and molecular markers (Adrian 1991). Those measurement techniques using particles as markers are grouped into the particle image velocimetry measurement (PIV) techniques.

Adrian (1991) identified three different operational modes for the PIV technique, depending on the mean number of concentration of scattering particles per unit volume: laser-speckle mode, particle-tracking mode, and high-image-density PIV mode. In the laser-speckle mode the image plane is overcrowded with the images of the tracer particles, and then particle overlapping generates random interference patterns known as laser speckle. The technique that measures the displacement of the laser speckle is known as laser-speckle velocimetry (LSV). When the particle-tracking mode, or low-image-density PIV mode, is employed, the particle concentration is low, and then particle overlapping is not probable. The particles, in general, are sparsely distributed on the image plane, allowing for tracking of individual particles. Here, the measurement of particle displacement is known as particle-tracking velocimetry (PTV). The high-image-density PIV mode occurs in between LSV and PTV. It is standard nowadays to refer to the high-image-density PIV mode simply as PIV.

When compared against other flow measurement techniques, PIV and PTV have the advantage of being non-intrusive and to provide full-field information. Then, the spatial resolution of these techniques is high. On the contrary, laser-Doppler anemometry (LDA) and hot wire techniques produce information on a single point in the measurement volume. Moreover, hot wire can introduce undesirable physical disturbance in the flow that could lead to measurement errors. On the other hand, the temporal resolution of LDA and hot wire are superior to PIV and PTV.

3.2. Particle image velocimetry

Particle image velocimetry is a full-field, non-intrusive velocity measurement technique that can obtain both qualitative and quantitative spatial and temporal information about a 2D flow velocity field. With PIV, the velocity is measured by recording the displacement of microscopically small neutral-density particles. Two or more short light pulses fired with a

known time separation illuminate these tracer particles, embedded in a volume of the flow. The images appear with spacing proportional to the local velocity vector. Therefore PIV is capable of producing instantaneous velocity maps. The problem, then, is to track and extract the velocity information quickly and accurately from the pattern.

It is well known that turbulent flows are 3D. For two-phase flows, the interaction between phases is also 3D. Consequently, any flow measurement technique considered for two-phase flow investigations has to be able to simultaneously determine the three velocity components. The extension of PIV to perform 3D measurements has been successfully achieved by acquiring Images from at least two cameras with different view angles. Then a stereo pair matching method is performed to determine the 3D position of a fluid particle in the viewing volume under study (Kasagi & Nishino 1991; Maas *et al.* 1993; Prasad & Adrian 1993; Costes *et al.* 1994; Hassan *et al.* 1998). Adamczyk & Rimai (1988) performed a 3D reconstruction from orthogonal views. For multiphase investigations, PIV can also be used if the different phases can be distinguished. Philip *et al.* (1994) used fluorescent seeds and special filters, by letting one camera to capture both phases and other camera in conjunction with the filter only capture the fluorescent seed images. Hassan *et al.* (1998) also differentiated between the phases by simply considering the size of the images. Transient information is also available since a series of pictures of the same area under study at many time steps can be taken.

Measurements performed with automated digital PIV are limited on the temporal aspect by the storage capability of the imaging boards and the RAM and hard drive of the computers. The spatial aspect is limited by the resolution, pixel size and array format, of the CCD cameras. These two limitations, however, are being overcome with the use of new technologies.

3.3. Hybrid particle tracking technique

Different tracking methods may be used to process the data. These include techniques such as cross-correlation (Hassan *et al.* 1992; Yamamoto *et al.* 1995), particle tracking velocimetry (Nishino *et al.* 1989; Malik *et al.* 1993; Wernet & Pline 1993), Spring Model (Okamoto *et al.* 1995), etc. Recently, new algorithms based on pattern recognition are becoming popular; among them neural networks, genetic algorithms, and fuzzy logic techniques seem to have good potential for particle tracking. There are different kinds of neural networks used in PIV. Grant & Pan (1995) used a Kohonen NN, while Hassan & Philip (1997) used an ART-2 NN technique. Yoon *et al.* (1997) employed a genetic algorithm for particle tracking. Fuzzy Logic techniques
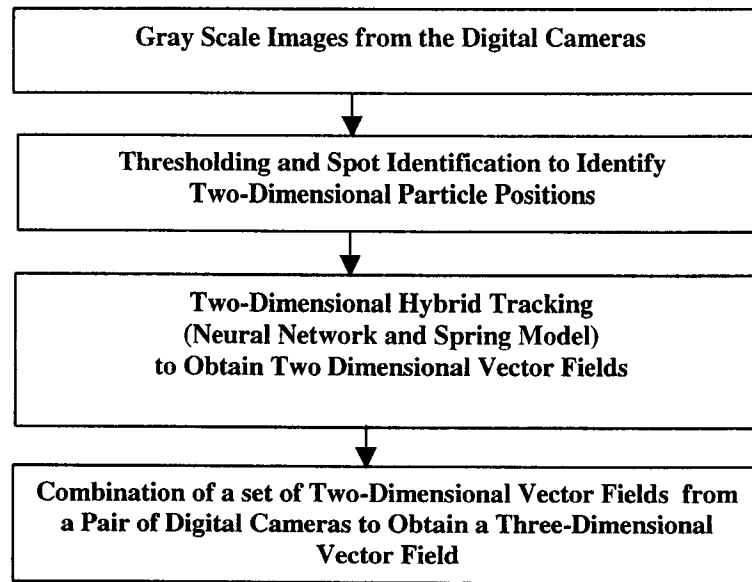
```
┌─────────────────────────────────────────────────────────┐
│        Gray Scale Images from the Digital Cameras         │
└─────────────────────────────────────────────────────────┘
                              │
                              ▼
┌─────────────────────────────────────────────────────────┐
│        Thresholding and Spot Identification to Identify   │
│              Two-Dimensional Particle Positions           │
└─────────────────────────────────────────────────────────┘
                              │
                              ▼
┌─────────────────────────────────────────────────────────┐
│               Two-Dimensional Hybrid Tracking             │
│             (Neural Network and Spring Model)             │
│            to Obtain Two Dimensional Vector Fields        │
└─────────────────────────────────────────────────────────┘
                              │
                              ▼
┌─────────────────────────────────────────────────────────┐
│   Combination of a set of Two-Dimensional Vector Fields   │
│     from a Pair of Digital Cameras to Obtain a            │
│          Three-Dimensional Vector Field                   │
└─────────────────────────────────────────────────────────┘
```

Figure 5. General process to determine the three-dimensional flow field.

have been employed by Wernet (1993).

The general process to determine the 3D flow field from the acquisition of the 2D images by the CCD cameras is outlined in figure 5. The recorded images are directly digitized via framegrabbers. Prior to employing the tracking routines, an initial processing stage is employed. The gray scales and the particle center of gravity are estimated. Then, a 2D hybrid tracking (in u, v coordinates) of the seed particle images is used. The need of a hybrid technique arises from the different flow patterns observed. The two tracking techniques used in this experimental study were an ART2 NN (Hassan & Philip 1997), and the Spring Model (Okamoto *et al.* 1995). The ART2 NN is an algorithm that self-organizes stable recognition codes (clusters) in real time in response to arbitrary sequences of input patterns, one at a time (Carpenter & Grossberg 1987). The Spring Model is a pattern recognition technique, which allows for tracking in rotating and shear flows.

In this hybrid-tracking algorithm, the particles are initially tracked with the ART2 NN, and then with the Spring Model. The ART2 NN tracks particles that present an alignment in four consecutive frames. Therefore, it allowed to perform Lagrangian measurements of the velocity

and acceleration of the liquid. Lagrangian measurements are required in the study of the forces acting on the bubble, as shown in Chapter VI. The ART2 was more successful in yielding velocity vectors mainly in regions away from the bubble. On the other hand, the Spring Model is a frame-to-frame tracking algorithm, which tracks a group of particles in two consecutive frames. The inclusion of this technique is necessary because it is not probable that the tracer particles will have the alignment property in the areas of turbulence, and in the bubble wake. As expected, the Spring Model yielded more velocity vectors in the wake of the bubble, and in areas of high turbulence. Once the tracking is performed, the data is combined, and repeated vectors are filtered out.

3.4. Matching of velocity vectors from stereo images

Before the three components of the position vector of any particle can be determined it is necessary to obtain information from two different views of the same particle. The criteria and algorithm to match velocity vectors from the stereo images are described next.

The process started by selecting a 2D vector tracked by the ART2 NN from four consecutive images (only two when the tracking algorithm employed is the Spring Model) acquired by the Center camera (CC). Then, the corresponding match vector was looked for among all the 2D vectors similarly tracked from images acquired by, say, the Right camera (RC). To consider a vector from RC being a possible match, it had to satisfy the following:

- The difference in the magnitude, in pixels, of the velocity in the v-direction, z-world coordinate, was less than a given tolerance ε_z, that is,

$$\left| \Delta v_C - \Delta v_R \right| \le \varepsilon_z. \qquad [8]$$

Observe that this is a direct consequence of that the three PIV cameras were positioned such that the v-coordinates coincide, as demonstrated by the camera calibration results, see Chapter II.

- The x-image coordinate of the possible match vector on the RC, u_R, was in a bounded range given by

$$u_{R\,min} - \varepsilon_x \le u_R \le u_{R\,max} + \varepsilon_x, \qquad [9]$$
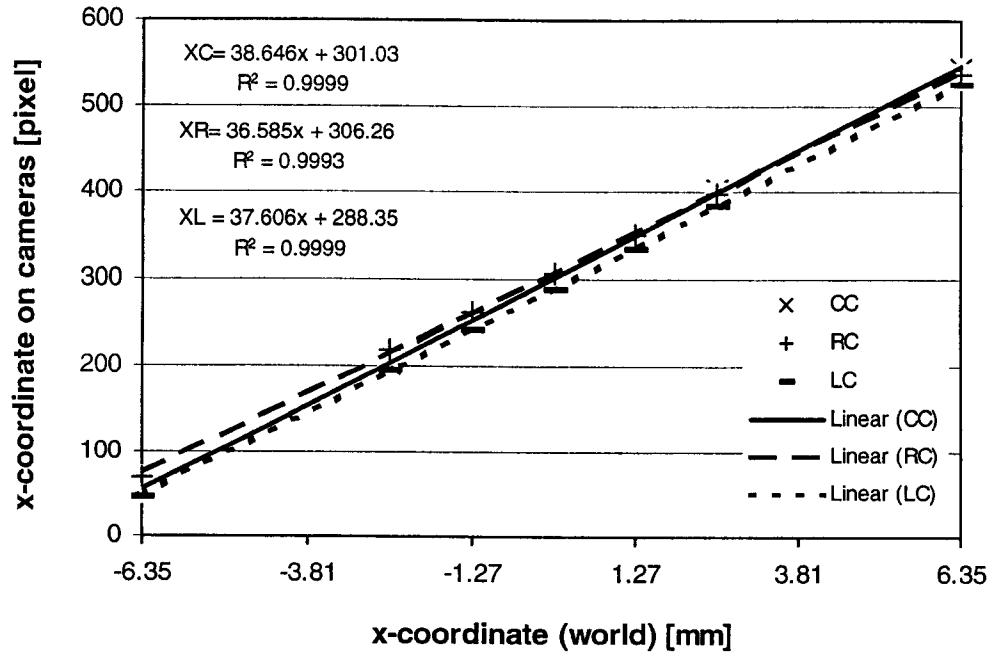
Figure 6. The variation of u for the PIV cameras against its world position, x, at $y = 0$. Also shown the results of application of a linear regression to the data points. See text for notation.

where ε_x is a tolerance. $u_{R\,min}$ and $u_{R\,max}$ depend on the y-world coordinate (the depth), and were determined as follows.

The x-world coordinate of the starting point of the 2D velocity vector tracked from images acquired by the CC was computed from the u_C and its corresponding linear regression performed with data from the CC, as shown in the figure 6. Observe that figure 6 can be used here because it was demonstrated in Chapter II that the image plane of the CC was practically parallel to the XZ-world plane.

Once x was calculated, the y range in which the starting point of the 2D velocity vector could fall into was calculated from

$$y^* = \pm\sqrt{r_0^2 - x^2},$$ [10]

where r_0 is the radius of the pipe. Then, x was also used to compute its corresponding

u_{R0}, at $y = 0$, from the corresponding linear regression performed with data from images from the RC, as shown in figure 6.

From figures 7a and 7b it can be seen that there was practically a linear dependence between the depth (y) and u_R and u_L for both the RC and the LC, respectively. Further, the values of the slopes were very close, for each respective camera. In fact, the standard deviation from the average value of the slopes was 0.262 and 0.277 for the RC and the LC, respectively. The average values of the slopes, say s_R and s_L, were -10.981 and 10.610 for the RC and the LC, respectively. The linear relation between y and u_R, and y and u_L, is a consequence of the high value of the focal length of the cameras (high zoom). s_R and u_{R0}, s_L and u_{L0} respectively, are the parameters defining completely a straight line, where the independent variable is y and the dependent variable is u. By evaluating this equation at y^* and $-y^*$, the $u_{R\,min}$ and $u_{R\,max}$, $u_{L\,min}$ and $u_{L\,max}$ respectively, in which the vector to match was located could be determined, for each respective camera.

All 2D-velocity vectors tracked from images acquired by the RC, LC respectively, that satisfied the two previous conditions were considered candidate match vectors to the originally chosen vector from the CC. To determine the real match vector, if any, the *epipolar geometry* (Ayache 1991; Mass *et al.* 1993) constrain was applied to every candidate vector.

The epipolar geometry constraint, in brief, indicates that for any point on an image, its corresponding match point on the corresponding stereo image lies on a line crossing the stereo image, but the precise location of the matching point on the line is unknown. The epipolar geometry is a very important condition used in robot and computer vision for the computation of the third coordinate from two 2D scenes, and it will not be covered here. The interested reader is referred to Ayache (1991) for a full description, and computational aspects. The epipolar constraint was employed here as follows. The distance between each of the component points, starting and end points, of the candidate velocity vector and its corresponding epipolar line were calculated. That candidate vector whose component points are closer to their epipolar lines was considered the winning matching vector. In the case of two or more vectors having one point close to its epipolar line, but the other point not so close, the vector whose magnitude in the *v*-component was closest to the reference vector from the CC was considered the winning vector.
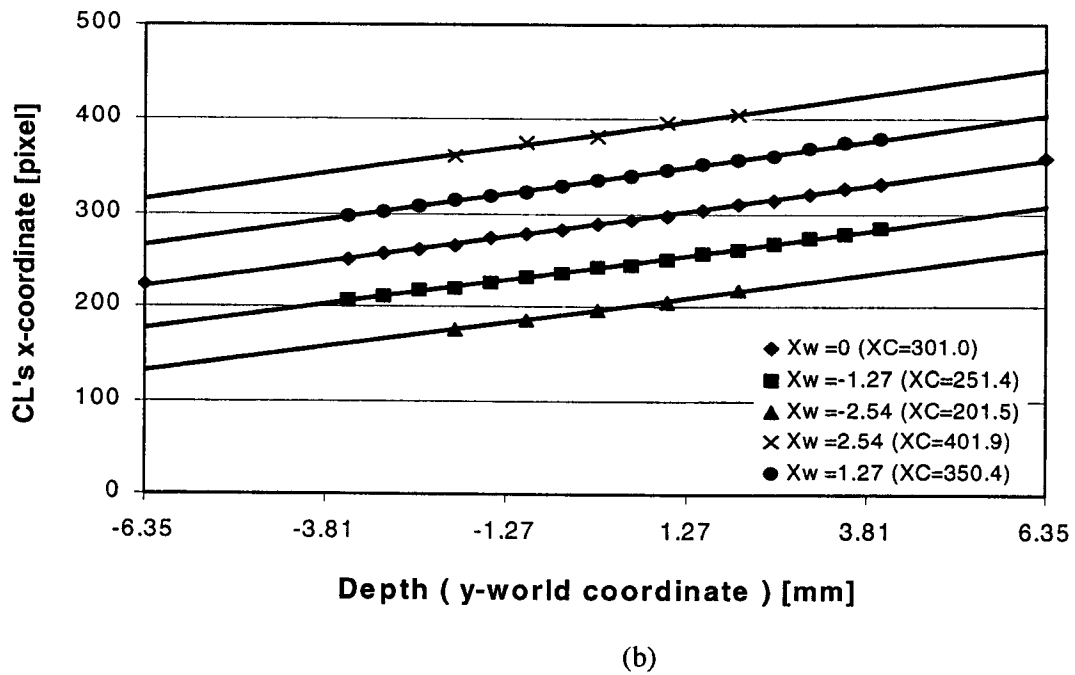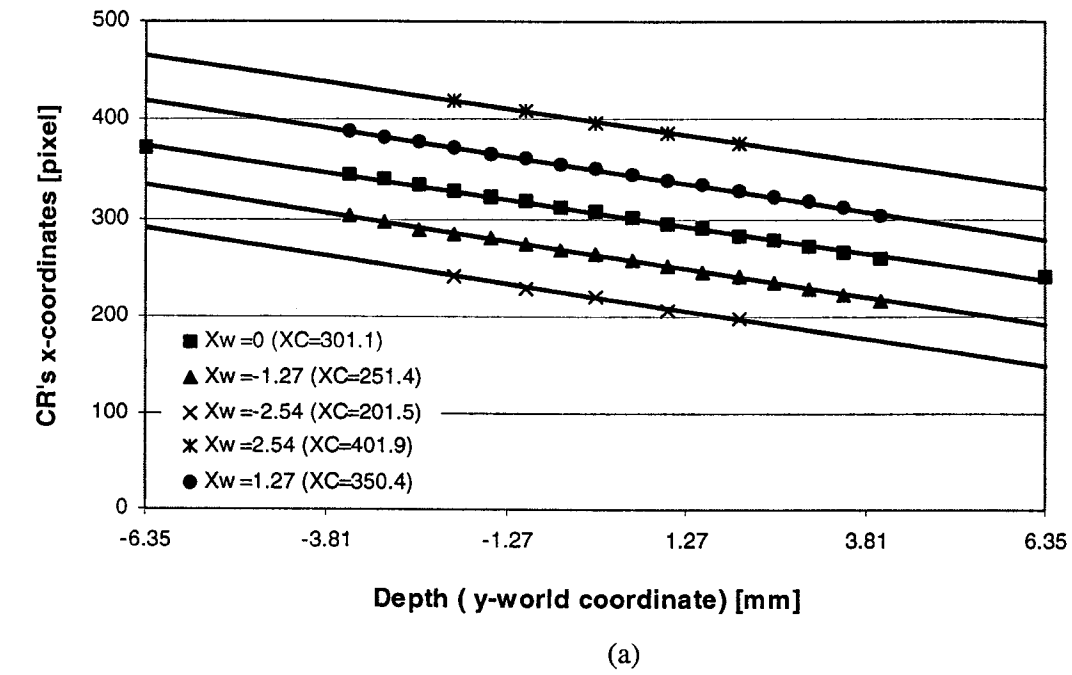
(a)

(b)

Figure 7. The variation of u respect to the depth, y, at different x positions. a) Data from the Right Camera; and b) data from the Left Camera. Also shown, the results of applying a linear regression to the data points.

Observe that in this process a matching of the 2D vectors was performed, and not individual particles. Therefore, the possibility of mismatching particles was highly reduced. Also, there was an important reduction of computational time, since there was no need to go through the whole process for all the particles on the images. Actually, only the starting point of the vector was used to look for candidate matches. Furthermore, when there was only one candidate vector, or none, the epipolar constraint was not necessary to be computed.

3.5. Determination of the three-dimensional position of the tracer particles

Once a 2D vector was matched between a pair of the three cameras, the 3D position of each individual seed particle was computed. For this calculation of the (x, y, z) world coordinates of the particle, the image coordinates of the particle from two cameras, say CC and RC, and the calibration coefficients for each camera are used in the perspective projective equations, [2] and [3]. The system of equations is casted as

$$
\begin{bmatrix}
t_{11R} - u_R t_{31R} & t_{12R} - u_R t_{32R} & t_{13R} - u_R t_{33R} \\
t_{21R} - v_R t_{31R} & t_{22R} - v_R t_{312R} & t_{23R} - v_R t_{33R} \\
t_{11C} - u_C t_{31C} & t_{12C} - u_C t_{32C} & t_{13C} - u_C t_{33C} \\
t_{21C} - v_C t_{31C} & t_{22C} - v_C t_{32C} & t_{23C} - v_C t_{33C}
\end{bmatrix}
\begin{bmatrix} x \\ y \\ z \end{bmatrix}
=
\begin{bmatrix}
u_R - t_{14R} \\
v_R - t_{24R} \\
u_C - t_{14C} \\
v_C - t_{24C}
\end{bmatrix}.
\tag{11}
$$

This overdetermined system of equations was solved by least squares, using the same algorithms described in Chapter II. The system is similar for the combination of the CC and the LC. The system is applied to every single particle belonging to a vector that could be matched between the CC and the RC, CC and LC respectively.

A schematic showing the whole process from tracking 2D vectors to the 3D position reconstruction is presented in figure 8. In this figure the 2D tracking correspond to the ART2 NN. Only two frames would be shown for the tracking with the Spring Model.
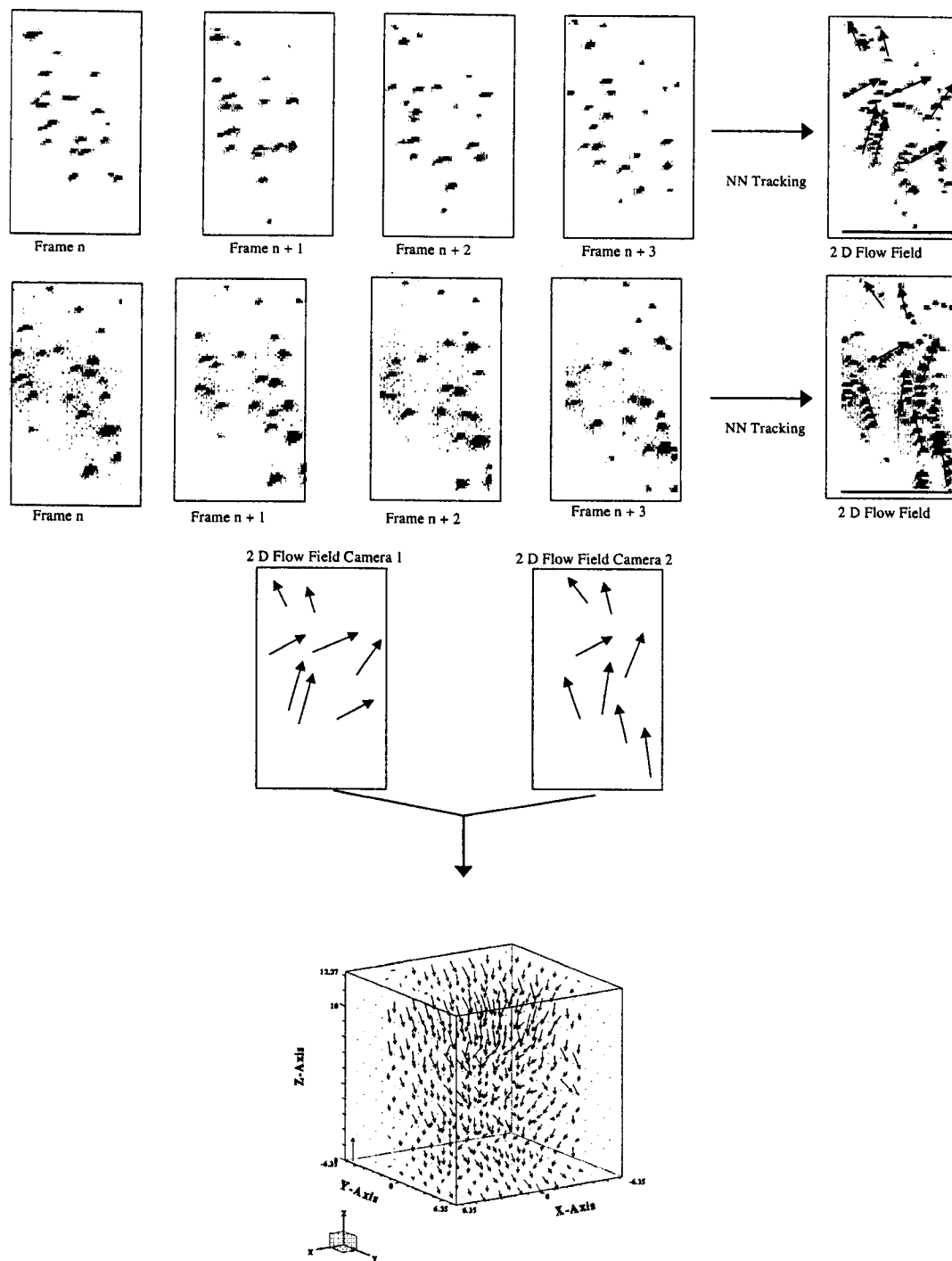
Figure 8. 3D stereoscopic reconstruction technique.

CHAPTER IV
BUBBLE SHAPE IDENTIFICATION AND RECONSTRUCTION

The behavior of a bubble moving in a liquid differs from that of a solid particle. The bubble shape can change due to the action of hydrodynamic forces. The interaction between rising gas bubbles and the surrounding fluid determines the shape of the bubble and the extent of the disturbance to the surrounding flow field. Instantaneous bubble shapes and sizes are important because they reflect the dynamic changes of their pressures inside the bubbles and in the surrounding fluid. Consequently, the velocity field changes of the surrounding fluid are also expressed. Bubble shape and dimensions play an important role in heat and mass transfer between the continuous and dispersed phases, since they determine the interfacial area available for such phenomena. Bubble volume and shape also affect the rise velocity and drag coefficient.

Experimental investigations have shown that small air bubbles are spherical or slightly ellipsoidal, and their rising motions are rectilinear. When their equivalent diameters increase, the bubble shapes will change to ellipsoidal (although not necessarily symmetric), and they will move along a zigzag or helical paths. If the equivalent diameter increases again, the bubbles will have a spherical-cap shape, and their motion becomes rectilinear again. The new trends in computational fluid mechanics (CFD) show that bubble shape could be predicted via direct numerical simulation from first principles, assumptions as potential flow, and some empirical correlations (Tomiyama 1998). To make such predictions reliable, experimental results are needed to provide systematic evaluation of surface interface response. The data available on bubble size and shape is by no means complete. Lui & Bankoff (1993) for example, have provided a comprehensive set of data on void fraction profiles and bubble chord length, but unfortunately no data on interfacial area concentration and bubble shape. Kataoka & Serizawa (1990) have provided interfacial area concentration data without bubble size and shape information.

The detailed information of bubble shape and size can only be obtained through visualization techniques. In this chapter, a technique that can reveal the full 2D projection of the shapes of bubbles rising in a liquid is presented. This technique is denoted the Shadow Particle

Image Velocimetry (SPIV). In conjunction with PIV, the measurement technique employed herein is a hybrid technique to identify the bubble shapes and velocity vectors.

4.1. Bubble detection in a bubbly flow

Multiphase flows can be easily studied by PIV, if the image of each phase is distinguishable. Several methods have been reported to separate the images resulting from different phases. The use of fluorescent tracers in the continuous phase as particle seeds is one way of solving this problem. With the aid of optical filters, one may separate the radiation scattered by fluorescent and neutral particles. In this process, one camera captures both phases. Another camera is equipped with a filter of the same wavelength of scattered radiation from the particles. Thus, it only captures the seed particle images. Then, by subtracting the images from both cameras the bubbles can be distinguished (Philip *et al.* 1994). This method of distinguishing phases also has the advantage that the camera equipped with the filter can identify the tracer particle images that overlap with the bubble images. Another method for identifying the phases considers the different image sizes or the gray levels of the seed particles and bubbles. The large difference in size and optical characteristic between tracer seeds and bubbles facilitates the flow phase discrimination (Hassan *et al.* 1998). This approach can be employed with or without applying the mask technique to a digital PIV record such that the images of particles that are either smaller or larger than a predetermined threshold value disappear from the image (Gui *et al.* 1996).

In this study, the size of bubble image was easily distinguishable from the images of the seeds as seen in figure 9a. From images like this one, at least the semiaxis of the bubble on the Z-direction can be determined, if an ellipsoidal shape is assumed for the bubble, or the radius, if a spherical shape is assumed. It also can provide the position of the center of the bubble in the Z-direction. Calculating the middle point between the two extremes of the bubble can estimate the center position. However, the uncertainty of the parameters can be significant. This is due to the strong reflection of the laser light on the bubble's surface does not allow for seeing the actual bubble boundary. On the X-direction, no reliable information can be inferred, since the bubble's edge is not visible. The position of the center of the bubble on the X-direction can be approximated by the u-coordinate of the centroid of the largest spot that is part of the bubble (the spot at top). Actually, this was the method used to determine the position of the bubble on the images acquired by the PIV cameras, and then permitting for an automated process to
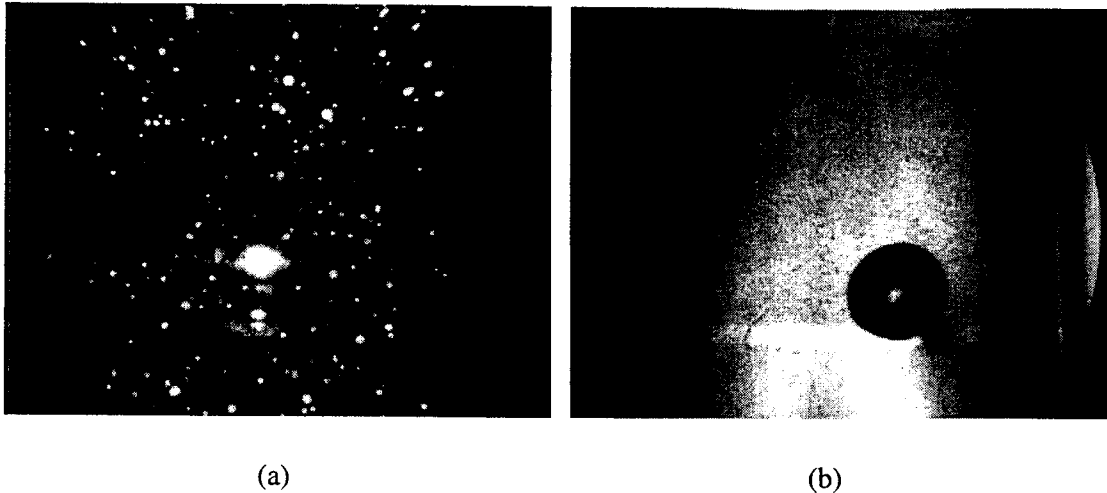
(a)   (b)

Figure 9. Typical simultaneous images acquired by the PIV and Shadow cameras when the bubble is present in the test volume. a) Image from the Center camera. It shows the XZ world plane; and b) image from the Shadow camera. It shows the YZ world plane. These two images allow for the three-dimensional reconstruction of the bubble shape.

determine bubble trajectories. Although the positions of the centroids of the bubble are approximations, it was found to be very close to the actual positions determined with the SPIV technique. Consequently, the averages of the flow fields performed under the condition that the bubble followed a particular trajectory were not affected, as explained later.

4.2. The shadow particle image velocimetry flow visualization technique

Three-dimensional analysis is required for bubbles' complicated shape and motion. This is due to the complex 3D (spirals or zigzags) bubble trajectories that do not remain in the light sheet (as in 2D PIV measurements) for a long duration. For 3D PIV measurements, a cone of light illuminated the viewing volume via two optic fibers, see figure 1. In this approach, the bubble images obtained showed only fragments of the bubble, and not the whole 2D projection shape, as shown in figure 9a. Sometimes, the bubble image shape even delineated a different shape from the natural bubble shape. This effect can be due to the change of scale and also to perspective distortion of the lens action, the lack of adequate illumination, or the intense light

reflection from the bubble.

To measure the bubble's shape, the PIV system was supplemented with a red shadow image technique. The shadow is produced by the reflected red light rays from light emitting diodes (LEDs), located opposite to one of the digital cameras, the S camera in figure 1. The light intensity from the LEDs is low, compared to the laser light. A red filter was placed in front of the S camera lens to only capture the bubble shadow. This high pass filter blocked the intense green light reflected by the bubbles. The corresponding shadow image of the rising bubble in figure 9a is presented in figure 9b. Both, figures 9a and 9b can be considered typical images.

4.3. Two-dimensional bubble shape reconstruction

It is clear that a bubble shape reconstruction process is necessary when 3D PIV measurements are performed. Even when the 2D shape is well defined, as provided by the SPIV technique, parameters such as orientation and dimensions still need to be computed. Several shape-identification and reconstruction techniques for distorted or incomplete images exist. They range from simply matching the image to a geometrical curve or surface, to the use of parametric curves or surfaces (as an example, Bezier and spline curves), and to the mapping of the original shape into a parametric space (such as the Hough transform). In the present study, a 2D image reconstruction process has been developed to determine both shapes and dimensions of the bubbles. This reconstruction method is based on the Dynamic Generalized Hough Transform (DGHT) algorithm, which is presented in detail by Leavers (1992). The DGHT algorithm is particularly useful when the object to be recognized and reconstructed is symmetric (e.g., circles, ellipses, etc.). Then, a 3D reconstruction can be achieved by combining two or more images obtained from cameras at different view angle.

Shape detection of fluid particles is often performed by visual inspection of photographic plates, since the resolution of the photographic film is much higher than digital recording systems. For the latter, image processing is a tool to improve the quality of the image. Computer vision techniques, such as thresholding, noise removal, edge detection, etc., are part of the image processing. The image analysis process of an image is divided into several steps (Hassan *et al.* 1998). The main steps of the reconstruction procedure were applied to figures 9a and 9b, and are described next.

- First, the images were expanded back to 640×480 format. This step was necessary because to achieve a framing rate of 60 Hz the resolution of the cameras was dropped by

half on the Y-direction. The algorithm used to expand the images consists in introducing a new line of pixels, which is a copy of the previous line of pixels. Figures 9a and 9b are images already expanded back.

- The second step applies a predetermined threshold value to the gray-scale digital image. Consequently, a binary image is obtained. The threshold operator is applied here because the processing algorithms are easier to implement using the resulting binary image (Davies 1990). The threshold value depends on the brightness of the image. In this step, most (and sometimes even all) of the noise (seeds included) can be dismissed, since usually the bubble image is much brighter than the seeds. Then, the resulting image is inverted. The result of this step can be seen in figure 10a and 11a, for the figures 9a and 9b, respectively

- Once the image is thresholded, a wide range of binary imaging operations becomes possible. These operators are applied on the resulting images from the previous operation. The third step consists of applying a size filter, which includes reducing and expanding algorithms. Here, the spot images are reduced. This reduction can be repeated for a predetermined number of times, so small spot images vanish. Afterwards, the remaining spot images are re-expanded until their original size and shape are restored (Davies 1990).

- The fourth step removes the remaining noise through a salt-and-pepper filter. This noise, basically due to electronic noise, appears as a light spot on a dark background or a dark spot on a light background. This filter fills small holes inside the big images, and also smoothes the object boundaries. The result of using the size and the salt-and-pepper filters is shown in figures 10b and 11b.

- The fifth step in this approach consists of detecting the edges of the bubble image boundaries. Figures 10c and 11c present the results of applying the edge-detection operator to figures 10b and 11b, respectively

- The last operation consists of determining the points that can be used as connectivity points. This step is critical; if the total number of connectivity points is small or of bad quality, any detection or reconstruction method will introduce a high degree of uncertainty in the estimated values of the required parameters. The connectivity points to be used in the reconstruction algorithm are shown in figures 10d and 11d. Clearly the images acquired by the shadow camera yield many and good-quality connectivity
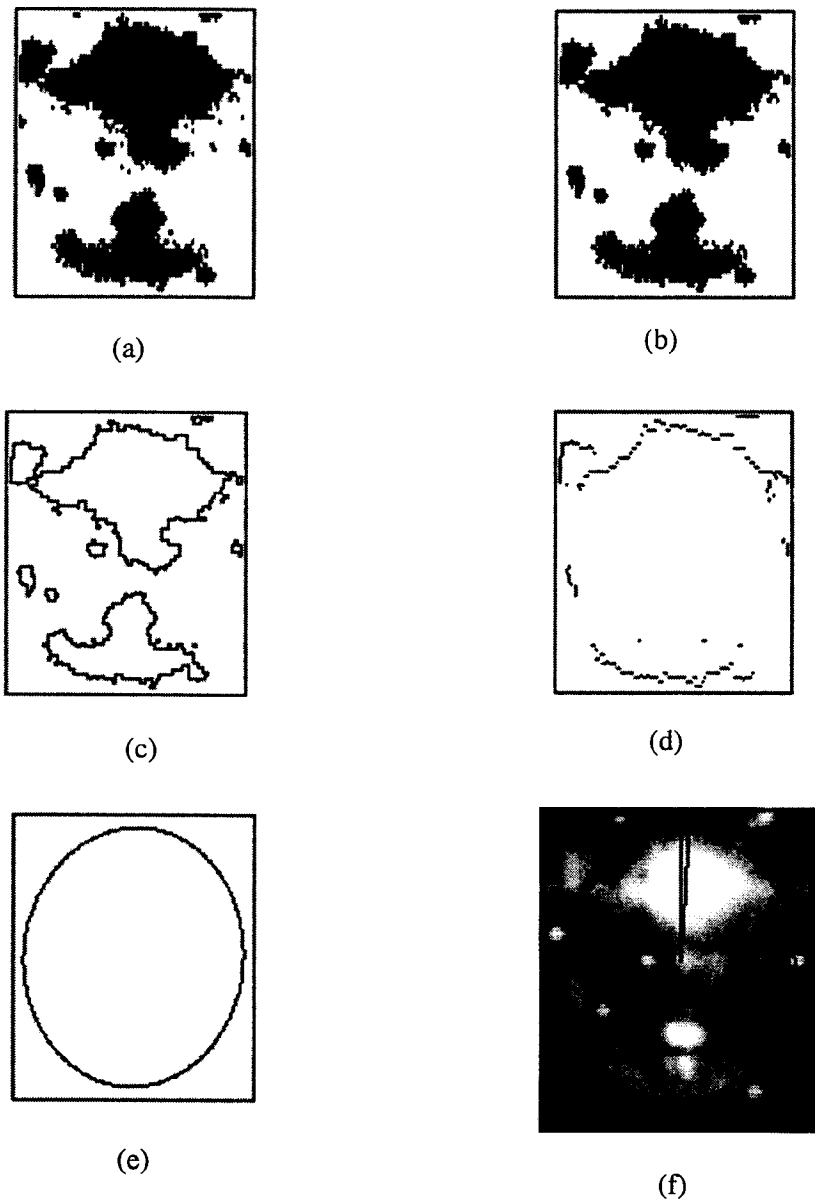
Figure 10. Bubble identification and reconstruction process for figure 9a. a) Binary image after applying the threshold and inversion operator; b) resulting image after applying size and salt-and-pepper operators to a; c) application of edge-detection operator to b; d) connectivity points to be used in the DGHT algorithm; e) the ellipse that best fits the connectivity points in d; and f) overlay of e and the original image. Also shown, the rotation angle with respect to the z-axis.
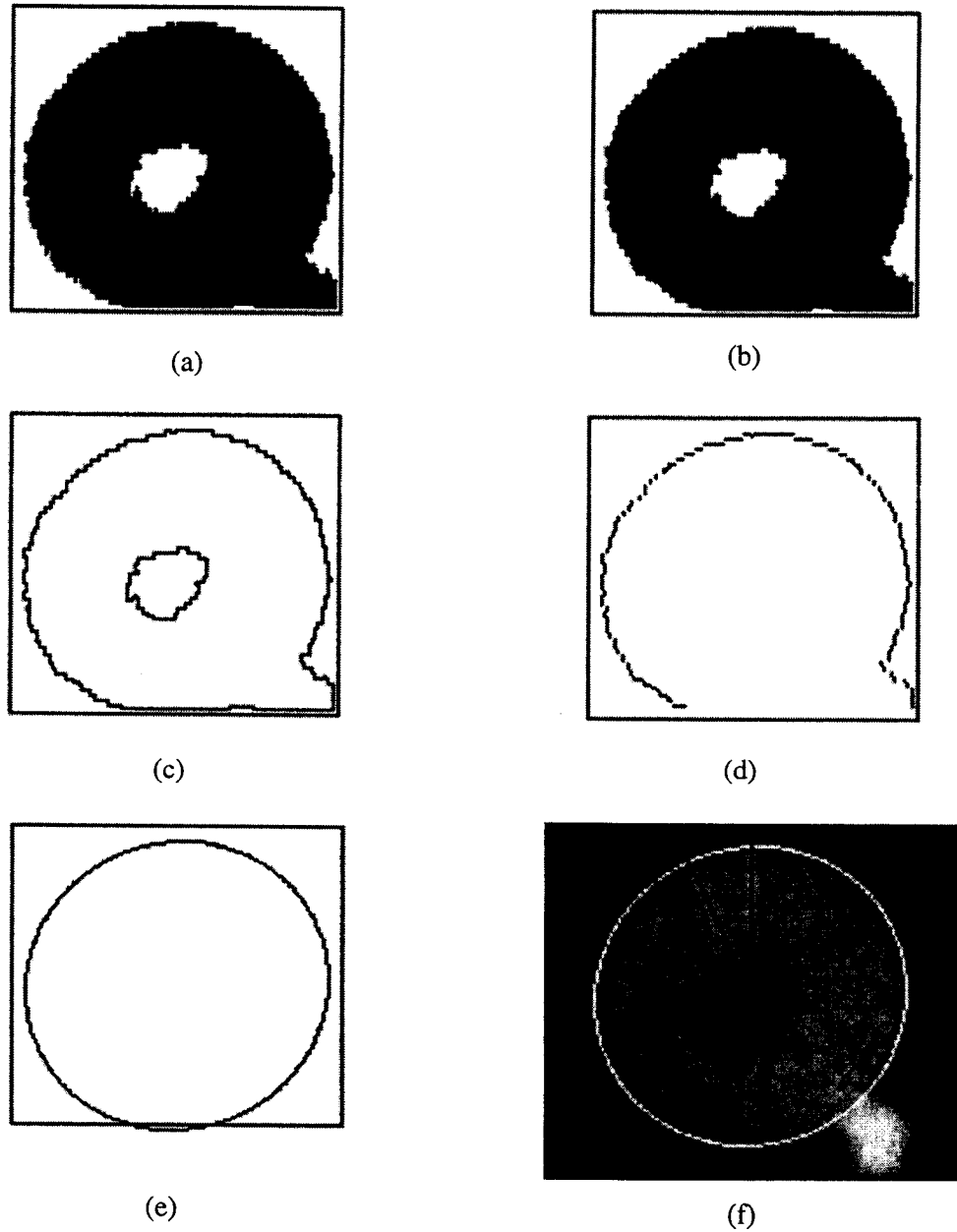
(a) (b) (c) (d) (e) (f)

Figure 11. Bubble identification and reconstruction process for figure 9b. a) Binary image after applying the threshold and inversion operator; b) resulting image of applying size and salt-and-pepper operators to a; c) application of edge-detection operator to b; d) connectivity points to be used in the DGHT algorithm; e) the ellipse that best fits the connectivity points in d; and f) overlay of e and the original image. Also shown, the rotation angle with respect to the z-axis.